Accepted to Astrophysical Journal
Preprint typeset using LaTeX style emulateapj v. 04/03/99

HIGH SPATIAL RESOLUTION X-RAY SPECTROSCOPY OF THE IC 443 PULSAR WIND NEBULA AND ENVIRONS

Douglas A. Swartz[1], George G. Pavlov[2], Tracy Clarke[3], Gabriela Castelletti[4], Vyacheslav E. Zavlin[1], Niccolò Bucciantini[5], Margarita Karovska[6], Alexander J. van der Horst[7], Mihoko Yukita[8,9], Martin C. Weisskopf[10]

Accepted to Astrophysical Journal

ABSTRACT

Deep *Chandra* ACIS observations of the region around the putative pulsar, CXOU J061705.3+222127, in the supernova remnant IC443 reveal an ∼5″-radius ring-like structure surrounding the pulsar and a jet-like feature oriented roughly north-south across the ring and through the pulsar's location at $06^h17^m5.200^s$ +22°21′27.52″ (J2000.0 coordinates). The observations further confirm that (1) the spectrum and flux of the central object are consistent with a rotation-powered pulsar, (2) the non-thermal spectrum and morphology of the surrounding nebula are consistent with a pulsar wind and, (3) the spectrum at greater distances is consistent with thermal emission from the supernova remnant. The cometary shape of the nebula, suggesting motion towards the southwest, appears to be subsonic: There is no evidence either spectrally or morphologically for a bow shock or contact discontinuity; the nearly circular ring is not distorted by motion through the ambient medium; and the shape near the apex of the nebula is narrow. Comparing this observation with previous observations of the same target, we set a 99% confidence upper limit to the proper motion of CXOU J061705.3+222127 to be less than 44 mas yr^{-1} (310 km s^{-1} for a distance of 1.5 kpc), with the best-fit (but not statistically significant) projected direction toward the west.

Subject headings: ISM: individual (G189.22+2.90, IC 443) — X-rays: individual (CXOU J061705.3+222127) — stars: neutron — supernova remnants — X-rays: ISM

1. INTRODUCTION

Pulsars lose their rotational energy in the form of magnetized relativistic winds. Being confined by their environment, these winds produce luminous pulsar wind nebulae (PWNe) with shapes and spectra determined by the pulsar emission geometry, magnetic field, and particle energy distribution as well as by the properties of the ambient medium and the motion of the pulsar relative to its surroundings (e.g., Kargaltsev & Pavlov, 2008). This is particularly true of pulsars still within their natal supernova remnant (SNR). PWNe evolve as they first expand into unshocked SN ejecta, then interact with the SNR reverse shock, the hot SN debris, and finally the surrounding interstellar medium (see, e.g., the review by Gaensler & Slane, 2006). Moreover, the pulsar may obtain a high space velocity at birth, move supersonically through its surroundings, and produce a cometary PWN with a bow shock that may be visible in X-rays and optical emission lines (Bucciantini, 2002).

A particularly intriguing example of the PWN phenomena is CXOU J061705.3+222127 (also known as G189.22+2.90 and as 1SAX J0617.1+2221; hereafter J0617) located at the southern edge of the SNR shell IC 443 where the shell interacts with a molecular cloud (e.g., Lee et al., 2008). This alignment suggests this PWN is entering a rare transitional stage where the overall morphology of the PWN is affected by its interaction with the SNR shell. While it shows a distinct cometary structure suggesting supersonic motion (Olbert et al., 2001; Bocchino & Bykov, 2001; Gaensler et al., 2006), the PWN is oriented ∼50° away from the direction expected if the pulsar originated at the center of the IC 443 remnant. This casts some doubt as to the physical association of this object and IC 443 as pointed out by Gaensler et al. (2006).

A hard, non-thermal, X-ray source located in the southern portion of IC 443 was first discovered by Keohane et al. (1997) with *ASCA*. The source was later observed with *BeppoSAX* (Bocchino & Bykov, 2000), with *XMM-Newton* (Bocchino & Bykov, 2001), and with *Chandra* for ∼10 ks using the Advanced CCD Imaging Spectrometer (ACIS) I-array (Olbert et al., 2001) and again for ∼37.5 ks using the S-array (Gaensler et al., 2006).

The latter three observations had sufficient angular res-

[1]USRA, Astrophysics Office, NASA Marshall Space Flight Center, ZP12, Huntsville, AL 35812, USA
[2]Department of Astronomy & Astrophysics, Pennsylvania State University, 525 Davey Lab, University Park, PA 16802, USA
[3]Remote Sensing Division, Code 7213, Naval Research Laboratory, 4555 Overlook Avenue, SW, Washington, DC, USA
[4]Instituto de Astronoma y Fsica del Espacio (IAFE, CONICET-UBA), CC67, Suc.28, 1428, Buenos Aires, Argentina
[5]INAF - Osservatorio Astrofisico di Arcetri, L.go E. Fermi 5, I-50125 Firenze, Italy; INFN - Sezione di Firenze, Via G. Sansone 1, I-50019 Sesto F.no (Firenze), Italy
[6]Smithsonian Astrophysical Observatory, MS 4, 60 Garden Street, Cambridge, MA 02138, USA
[7]Department of Physics, The George Washington University, 725 21 Street NW, Washington, DC 20052, USA
[8]The Johns Hopkins University, Homewood Campus, Baltimore, MD 21218, USA
[9]NASA Goddard Space Flight Center, Code 662, Greenbelt, MD 20771, USA
[10]Astrophysics Office, NASA Marshall Space Flight Center, ZP12, Huntsville, AL 35812, USA

olution to study the pulsar[11] and many details of the PWN and surroundings. All three studies noted the soft thermal spectrum of the central point source is consistent with emission from the surface of a neutron star. Olbert et al. (2001) first identified the comet-shaped morphology of the nebula and argued it could be explained by supersonic motion causing a pulsar wind to terminate in a bow shock and flow downstream in a synchrotron tail. The deeper observation obtained by Gaensler et al. (2006) revealed a surface brightness plateau extending to $\sim 25''$ downstream of J0617 which they interpreted as the backward termination shock. They used the locations of the forward and backward shocks to deduce a low Mach number, $\sim$1.2, for the flow and argued this was indicative of motion through relatively hot (shocked) supernova debris. Gaensler et al. (2006) also identified two compact knots of emission a few arcseconds north and south of J0617. Bocchino & Bykov (2001) showed that the hard power-law spectrum at the core of the nebula softens with distance from J0617 and is consistent with synchrotron cooling models.

Here, analysis of a much deeper, $\sim$152 ks, ACIS S-array observation is presented. An overview of the observation and data reduction methods is given in Section 2 followed by analysis of the X-ray morphology, a comparison of the X-ray to optical emission line images, and analysis of the X-ray (and radio) spectrum at high spatial resolution (Section 3). The bright source, J0617, is confirmed to display the physical properties of a pulsar (though no pulsations are detected) that powers a bright, cometary-like, roughly $2'\times1.5'$ PWN. Within the nebula is a nearly circular, $\sim 5''$ radius, ring of enhanced X-ray emission enclosing a jet-like feature oriented roughly north-south and passing through the position of J0617. The results are then interpreted (Section 4) in terms of synchrotron emission from relativistic particles generated by the pulsar and confined by the surrounding medium.

A distance of $d = 1.5$ kpc ($1'$=0.42 pc) to J0617 is adopted following Welsh & Sallman (2003) but note, as pointed out above, there remains some doubt as to the physical association of J0617 and the SNR IC 443. Therefore, distances are given in units of $d_{1.5} = d/1.5$ kpc where appropriate.

2. DATA & METHODS

2.1. *X-ray Observations*

J0617 was observed with the *Chandra* X-ray Observatory Advanced CCD Imaging Spectrometer on 2012 February 6 (ObsID 13736) for $\sim$107.6 ks and again on 2012 February 8 (ObsID 14385) for 44.5 ks. Both observations used an identical instrument configuration which placed J0617 near the back-illuminated CCD (S3) aimpoint. The observations were taken in full-frame timed exposure mode using the standard 3.2 s frame time and the VFAINT telemetry format.

The data were reprocessed using the Chandra X-ray Center script `acis_process_events` (CIAO v. 4.5) to apply the latest time-dependent gain correction (CalDB 4.5.5) and to flag potential cosmic-ray background events. Only events imaged on the back-illuminated CCD S3 are used in this work. Point-like X-ray sources in the field were identified using the source-finding utility in the `lextrct` image-analysis program (Tennant, 2006). The locations of sources identified in the two event lists were compared and were found to be in sufficient agreement for most purposes so that the two event lists were simply combined using the FTOOLS utility `fmerge` to produce a 152 ks duration final event list. In addition, a sub-pixel image was created by rebinning the events to 1/2 of the nominal ($0.492''$) ACIS pixel size in order to examine the finer details of the X-ray morphology in the immediate vicinity of J0617 (section 3.1.2).

Spectral fitting reported here uses the XSPEC, v. 11.3.2g, spectral-fitting package (Arnaud, 1996). Spectral redistribution matrices and ancillary response functions were generated using the CIAO tools `mkacisrmf`, `mkarf` and `mkwarf`. Spectral analysis is confined to events within the 0.5−8.0 keV energy range. The energy range spans only 0.5−5.0 keV in those cases where a soft thermal-dominated spectrum produces a negligible number of high-energy source counts as is the case outside the PWN region.

The X-ray surface brightness and X-ray color or hardness ratio vary noticeably across the $\sim 8'\times 8'$ S3 field of view. The 'contour binning' method of Sanders (2006) was therefore applied to the merged data set in order to map the physical properties, deduced from spectral model fitting, in the regions containing J0617, its PWN, and portions of the surrounding diffuse thermal plasma. The contour binning method defines spatial bins (for spectral analysis) which cover contiguous regions of similar surface brightness and is motivated by the fact that surface brightness variations often follow changes in physical properties, such as those at shock fronts, in the X-ray-emitting medium.

For this purpose, the identified point sources were first removed from an image constructed from the merged event list and back-filled with a sampling of the adjacent background using the CIAO tools `roi` and `dmfilth` following the diffuse emission science thread.[12] The resulting image was then accumulatively smoothed using a signal-to-noise ratio threshold of 30 and contour-binned using a signal-to-noise threshold of 100 using the `accumulate_smooth` and `contbin` utilities, respectively, from Sanders (2006).

An earlier observation of J0617 (ObsID 05531), taken 2005 January 12 using a similar instrument configuration, is used in analysis of the proper motion of J0617 (section 3.1.1).

2.2. *Optical Observations*

The analysis presented here also makes use of Hα and [OIII] images obtained 23 Nov 2012 using the Astronomical Research Cameras[13] E2V 230-42 CCD ($\sim 0.493''$ pixel^{-1}) mounted on the 0.9 m Southeastern Association for Research in Astronomy telescope at Kitt Peak Observatory. Seeing conditions were $\lesssim 2''$. Contemporaneous R and V images were used for continuum subtraction from Hα and [OIII], respectively. The continuum-subtracted images were registered to the X-ray data using 2MASS objects

[11] A pulsar is inferred by the nature of its X-ray properties although no pulsations have yet been observed from the compact object.

[12] http://cxc.harvard.edu/ciao/threads/diffuse_emission/

[13] http://www.astro-cam.com

common to both wavelengths.

2.3. *Radio Observations*

Archival observations of IC 443 at 330 MHz, 4.8 GHz, and 8.4 GHz, obtained with the Very Large Array (VLA),[14] were also analyzed and compared to the X-ray data. All data were calibrated and reduced using the Astronomical Image Processing System (AIPS) data reduction package[15].

Multiple 330 MHz observations were carried out from 2005 to 2007 using several VLA configurations (Castelletti et al., 2011) so that the final combined image is sensitive to a wide range of spatial structures from $\sim 6''$ up to $\sim 70'$ and therefore samples both the PWN and the surrounding extended IC 443 SNR. See Castelletti et al. (2011) for further details of the 330 MHz observations and data reduction. The final combined image has an angular resolution of $17''$ and a background noise level of 1.7 mJy beam^{-1} after correcting for primary beam attenuations. The average SNR contribution in the region surrounding J0617 is 15 mJy beam^{-1}.

The 4.8 GHz observation was taken in the C configuration on 1997 August 26 and the 8.4 GHz observation in D configuration on 1997 December 31. The 4.8 GHz observation was taken with two 50 MHz tunings centered at 4.8851 GHz and 4.8351 GHz and the 8.4 GHz observation was taken in two 50 MHz bands centered at 8.4351 GHz and 8.4851 GHz. Both observations used 3C 138 as the flux calibrator and 0632+103 as a phase calibrator. These observations were first analyzed by Olbert et al. (2001). These data are only sensitive to structures on scales up to a little over $2'$ and thus are not able to sample the emission over the entire nebula as is possible at 330 MHz. Here, they were re-calibrated and reduced using standard data reduction techniques applied within AIPS. The data were self-calibrated in two rounds of phase-only calibration. The final, full resolution, 4.8 GHz image rms is 0.18 mJy beam^{-1} with a beam size of $\sim 5.5'' \times 3.8''$ and the 8.4 GHz image rms is 0.076 mJy beam^{-1} with a beam size of $\sim 8.1'' \times 7.1''$.

3. RESULTS

3.1. *General X-ray Morphology*

The deep *Chandra* image (Figure 1) reveals J0617 as the brightest point-like object in the field surrounded by a high-surface-brightness nearly-circular ring. There are two 'spokes' apparently connecting J0617 to the ring oriented roughly north-south which are possibly pulsar jets. Exterior to the ring is a comet-shaped nebula with its major axis oriented $\sim 50°$ East of North and with its apparent forward direction to the Southwest. The cometary nebula has a hard X-ray spectrum as was noted by Olbert et al. (2001) and Gaensler et al. (2006). Predominantly soft X-ray emission surrounds the roughly $2' \times 1.5'$ cometary nebula and extends throughout the S3 field of view (along with a few faint unrelated point-like sources). The surface brightness of this extended emission is spatially non-uniform varying by factors of 4 to 5 over spatial scales of order $1'$. As shown by spectral analysis (section 3.2), this extended diffuse emission is primarily thermal in nature whereas the cometary nebula, ring, and related features are dominated by hard non-thermal spectra.

Analysis of these features is discussed in greater detail in the following subsections beginning with an estimate of the proper motion of J0617.

3.1.1. *Constraints on the Proper Motion of CXOU J061705.3+222127*

The current observations were taken 2582 ± 1 days since the 37.5-ks observation ObsID 05531 was taken with J0617 at the aimpoint. An earlier *Chandra* observation, ObsID 00760, was too short to be useful for precise measurements of proper motion. Four point-like X-ray sources, in addition to J0617, were identified common to both ObsID 05531 and the deeper of the two recent observations, ObsID 13736. The spectra of three of these four sources have significant fractions of their counts above 2 keV indicating a high relative probability that they are distant background objects and hence fixed on the plane of the sky. The fourth source is softer and possibly a foreground star. It is listed in the USNO-B1.0 Catalog (Monet et al., 2003) with designation 1123-0129324 with a negligible proper motion. Offsets (independently in R.A. and Decl.) between the two observations were computed by minimizing the error-weighted separations among the four sources. After applying these relative astrometric corrections, the 99%-confidence contour extremum sets an upper limit to the proper motion $\leq 310 d_{1.5}$ km s^{-1} with the best-fit (but not statistically significant) direction toward the west. Specifically, the estimated motion is -22.3 ± 33.9 mas yr^{-1} in R.A. and -0.1 ± 33.9 mas yr^{-1} in Decl.

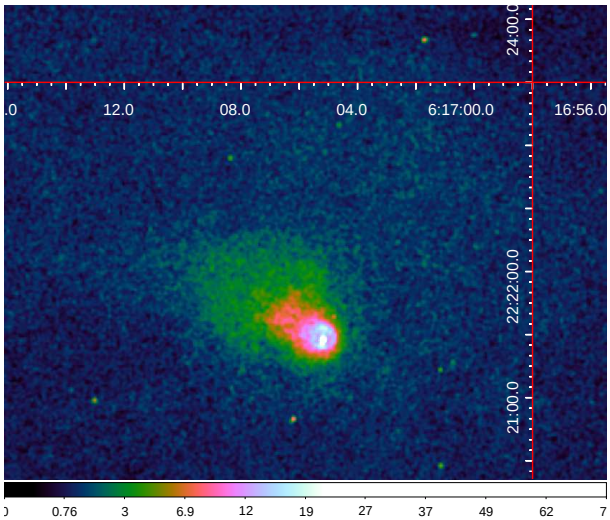

FIG. 1.— X-ray image from the merged, 152 ks duration, *Chandra*-ACIS observation restricted to the 1.0−5.0 keV energy range and covering a $4.75' \times 3.75'$ region near the aimpoint and smoothed using a Gaussian kernel of 3 pixel ($1.48''$) radius. Colors are proportional to the number of X-ray events per pixel using a square root scaling. CXOU J061705.3+222127 is the bright white object surrounded by a ring (light blue) and the comet-shaped PWN (red and green). Relatively low surface brightness structure (dark blue to black) is visible throughout the S3 field of view. The center of the IC 443 supernova remnant lies $\sim 30'$ to the N of J0617.

[14] The Very Large Array of the National Radio Astronomy Observatory (NRAO) is a facility of the National Science Foundation operated under cooperative agreement by Associated Universities, Inc.

[15] http://www.aips.nrao.edu

3.1.2. *J0617, the Jet, and the Ring: Subpixel Imaging*

Figure 1 displays the 2.0−4.0 keV subpixel-sampled region around J0617 including the ring-like and jet-like structures. This energy range best distinguishes the ring from other features and mutes the contribution from J0617 which is brightest at lower energies (section 3.2.2). Figure 2 shows the broad-band surface brightness radial profile centered on the position of J0617, extending to 12.3″, and including only azimuthal angles between PA 200° and 340° (±70° of West) in order to avoid contributions from the jet-like features. This profile was obtained from the 1/2-pixel sampled image. Also shown is a model point spread function for a monochromatic source at 2.5 keV generated using the Chandra Ray Tracer (ChaRT) and MARX simulation tools. The ring appears as the peak at 4.8″ with a (Gaussian) width of 1.2″. These parameters were estimated by fitting the surface brightness profile with a combined power law plus Gaussian function. Another peak in the radial profile appears between J0617 and the ring. This feature is about 1″ from J0617 but adding an additional Gaussian component shows this feature is not statistically significant.

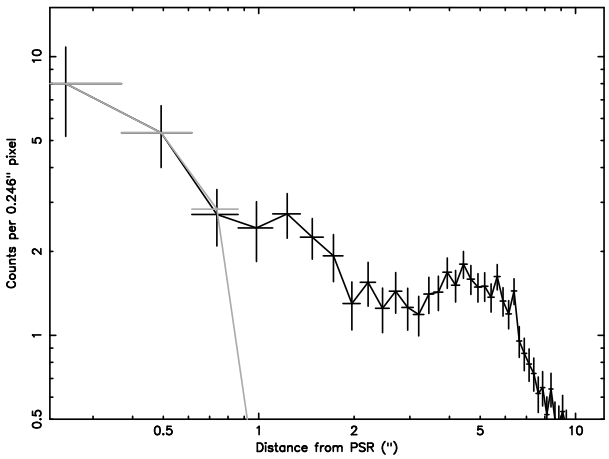

FIG. 2.— X-ray brightness radial profile centered on J0617 and restricted to azimuthal angles on the PA range 200° to 340° (±70° of due W). The vertical scale is the number of counts per 0.246″×0.246″ ACIS CCD subpixel detected in the 2.0−5.0 keV bandpass. The thin line is a ChaRT model of a 2.5 keV monochromatic point source.

The jet-like feature spans from the position of the pulsar northward and southward until it appears to intersect the ring. The ring brightens at these intersections. These intersections were described as compact emission components by Gaensler et al. (2006). The southern jet feature has a surface brightness about 75% higher than the northern jet in the 0.5−8.0 keV energy range.

The center of the ring is not coincident with the location of J0617. A spatial model representing an annulus was fit to the sub-pixel X-ray image in the 2−4 keV energy range after ignoring data within a 2.5″ radius of the center of the ring (due to the brightness of the pulsar) and smoothing the data slightly (Figure 3). The model consists of two elliptical Gaussians plus a constant where one Gaussian has a positive amplitude and the other a negative amplitude in order to approximate an elliptical annulus. The location of the centroid of the ring model is $06^{\rm h}17^{\rm m}05.166^{\rm s}$ $+22°21'28.80''$. This location is offset by 2.7″ ($0.06d_{1.5}$ ly) from J0617 at PA∼340°, i.e., the pulsar is roughly SSE of the ring center. The ring is close to circular. The best-fitting parameters result in an aspect ratio of 0.86±0.05 and an angular eccentricity, $\cos^{-1}(b/a) = 30.7 \pm 5.6$ deg where a and b are the major and minor Gaussian widths. The PA is 84±3 deg; the ellipse major axis is nearly in the east-west direction.

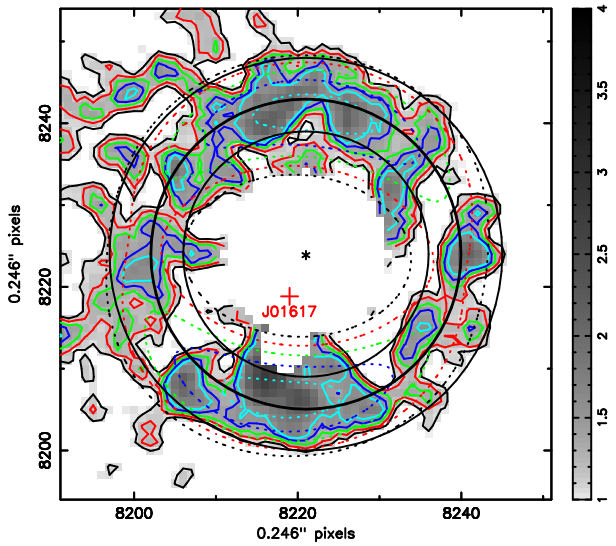

FIG. 3.— X-ray subpixel image of the ring surrounding J0617 restricted to the 2.0−4.0 keV energy range and to the region within ten pixels (∼2.5″) of the center of the ring (including the pulsar) excluded. Solid contours indicate counts pixel^{-1} in the data and range from 1.05 to 1.55 in steps of 0.125. Dotted contours indicate model fits to the ring morphology using the same range of levels. The model is the sum of two elliptical Gaussians, one with a positive amplitude and one with a negative amplitude (together approximating an annulus), and a constant. All parameters (centroids, widths, amplitudes, and position angles of the Gaussians and the constant) were allowed to vary in the fitting although the centroids of the two Gaussians were tied to the same values. Circles are shown centered on the best-fit centroid (denoted by the asterisk) and show that the overall shape of the ring is close to circular. The position of J0617 is denoted by the red cross.

3.1.3. *Morphology of the Pulsar Wind Nebula*

Figure 4 displays the 0.5−8.0 keV brightness profile along the major axis (PA 50°) of the comet-shaped PWN. The profile has been averaged over a ±30″ region perpendicular to this axis. The peak of the profile coincides with the pulsar and offsets upstream of the pulsar (toward the southwest) are taken as positive in this figure. The ring is clearly visible as secondary peaks on either side of the pulsar. The profile >5″ upstream of the pulsar decreases smoothly out to at least 2′ from J0617 without any discernable structural features. As with the upstream profile, the downstream profile first declines steeply from the exterior of the ring but then it reaches a broad peak extending from 15″ to 25″ away from the pulsar. The profile then declines more slowly out to approximately 2′ downstream without any additional features.

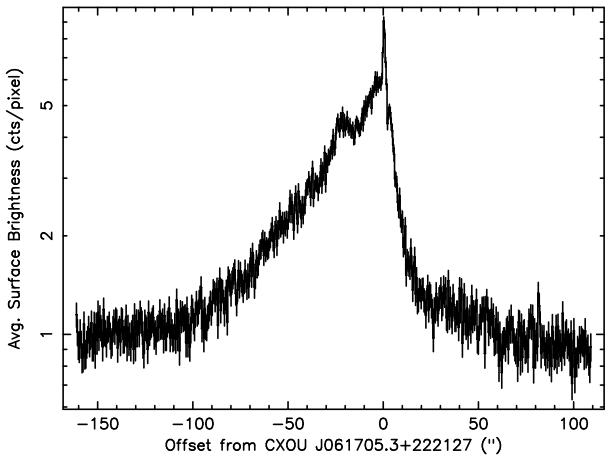

FIG. 4.— X-ray brightness profile along the major axis of the PWN. Upstream is to the right. The vertical scale is the number of counts per 0.492″×0.492″ ACIS CCD pixel detected in the 0.5−8.0 keV bandpass in a 60″ wide strip oriented perpendicular to and centered on the major axis.

The X-ray image does show that the surface brightness distribution upstream of the pulsar is bow-shaped. Parabolas were fit, by visual inspection, to the surface brightness contours in the upstream region of a smoothed image (with the ordinate axis of the parabolas constrained to be parallel to PA 50°) as shown in Figure 5. The parabolas are of the form $(y/d_s) = 0.54(x/d_s)^2 + 1$ where d_s is the distance from the location of J0617 (at the focus) to the vertex of the parabola.

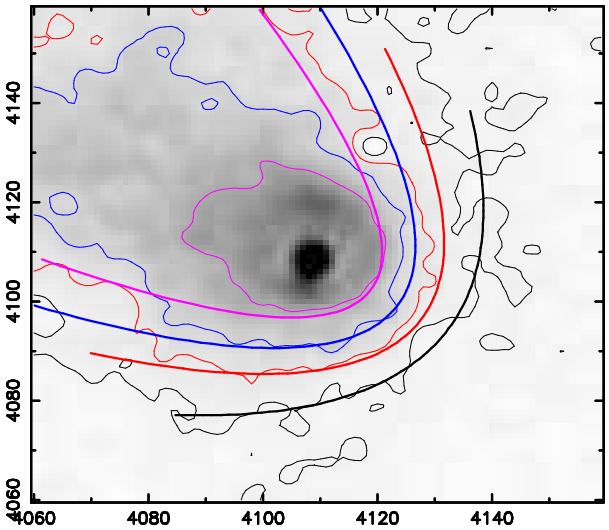

FIG. 5.— X-ray image of the upstream region around the PWN. The image has been smoothed by three applications of a nearest-neighbor smooth. Contours are drawn at levels of 1.5, 3.0, 5.0, and 10 c pixel^{-1}. Corresponding (color-matched) curves are parabolas parameterized by visual inspection to represent the contours. The parabolas are constrained to have their ordinates parallel to the apparent line of motion of J0617 at PA 50°.

There is no evidence for a bow shock in either the Hα or [OIII] images of this region and there is little or no correlation between the X-ray emission in the upstream direction with the optical line emission. However, as a close-up image of the region shows (Figure 6), there is Hα emission coincident with the jet-like X-ray feature. This is likely an accidental coincidence as there are many similar Hα features throughout the IC 443 SNR. Similarly, there is also a well-defined Hα wisp downstream of J0617 that runs roughly along the major axis of the PWN and thins in the downstream direction (Figure 7). This feature is also visible in the [O III] image. There is no X-ray feature correlated with this wisp. Although its location is suggestive, it is unclear if this Hα wisp is related to the PWN as there are numerous wisps with similar morphology throughout the region that are obviously not related to the PWN proper.

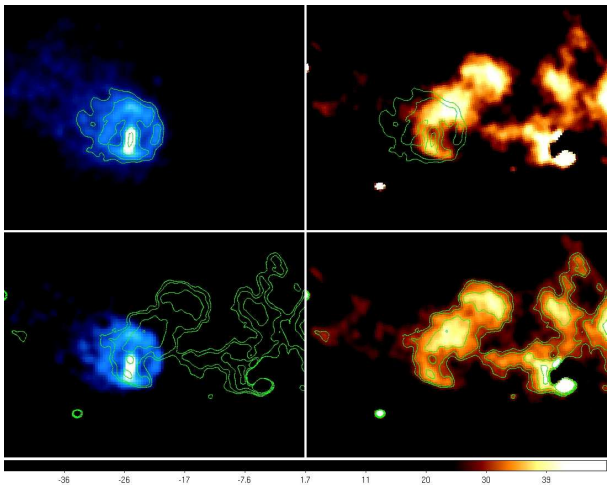

FIG. 6.— Detail of the ring and jet-like features in X-ray (left two panels) and Hα (right two panels) with X-ray contours (top panels) and Hα contours (bottom panels) overlaid. Panels sizes are 1′×0.75′.

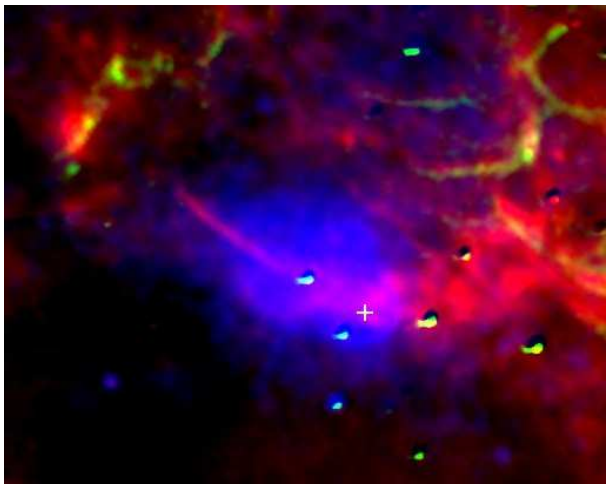

FIG. 7.— X-ray (blue), Hα (red), and [OIII] (green) color composite of a 4.2′×3.4′ portion of the IC 443 field. The location of J0617 is marked with a white cross. Note the Hα wisp extending east-west roughly along the line of apparent motion of J0617 superimposed on the PWN.

3.2. *X-ray Spectroscopy of Major Structures*

3.2.1. *Regions Exterior to the PWN: Background SNR*

Customarily, a background region is selected from those regions remote from the primary source, in this case the PWN, in order to isolate the source spectrum for analysis. However, J0617 is located along the line of sight through the extended X-ray emission associated with the SNR IC 443 and this emission is highly non-uniform as noted above. Several regions were visually selected and analyzed

to quantify the spectral properties of this "background" throughout the field of view of the S3 chip. These regions are numbered 1 through 9 in Figure 8 and their spectra are shown in Figure 9. Assuming this emission is from hot plasma within the SNR, the observed variations may be due to a combination of different plasma temperatures, emission measures, elemental abundances, and intervening absorption. The simplest model that can account for all these variables in XSPEC is an absorbed optically-thin thermal plasma model. The spectral analysis reported in this section is limited to the range 0.5−5.0 keV because of the paucity of source photons above 5 keV.

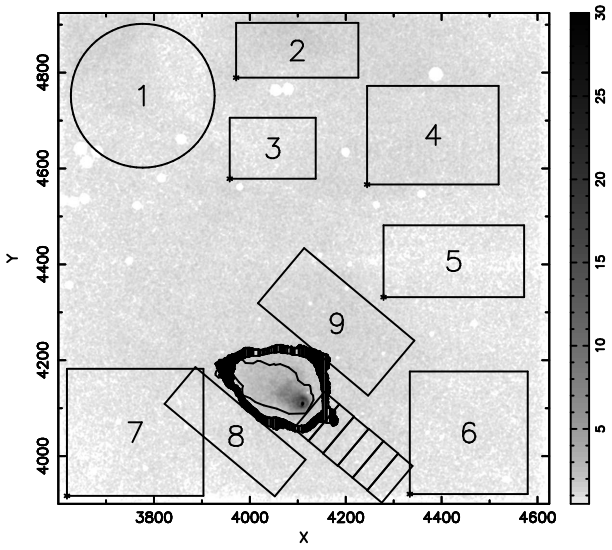

FIG. 8.— Regions selected for spectral analysis of extended emission. Numbering corresponds to the region numbers in Table 1. Additional small rectangular regions upstream of J0617 are analyzed in section 3.2.4. The thick irregular region around J0617 delineates the outermost of 7 high-surface-brightness PWN regions investigated in section 3.2.5 and the thin inner irregular region defines the radio-bright region analyzed in section 3.2.6.

It was found that the spectra of these 'outlier' regions cannot be fit satisfactorily with a single-component absorbed (XSPEC model `phabs`) variable-abundance thermal emission (`vmekal`) model. A significant improvement could be made by adding either a second thermal component or a power law (`powlaw`) component.

Resulting best-fit model parameters are listed in Table 1 for these outlier fields. These include the absorption column density, $n_{\rm H}$, the power law index, Γ, the thermal component temperature, kT, the model component normalizations, K[16], the 0.5−5.0 keV flux, f, in erg cm^{-2} s^{-1} (uncorrected for absorption) and the χ^2 fit statistic and number of degrees of freedom, dof. Here and elsewhere errors are 90% confidence extremes for a single interesting parameter unless otherwise noted.

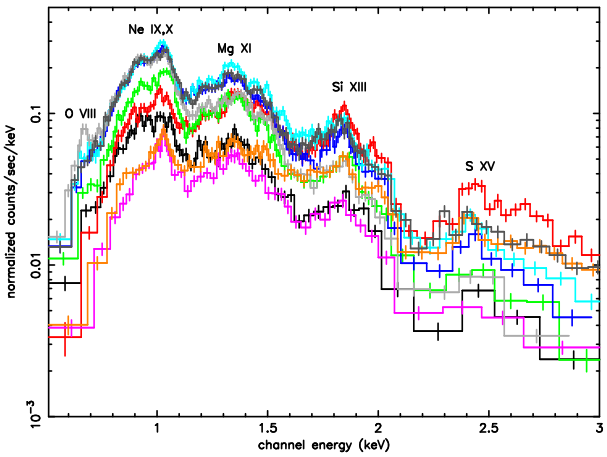

FIG. 9.— Observed spectra of the 9 numbered regions shown Figure 8. The spectra have been binned up to 10 channels in order to achieve a minimum detection significance of 10 for display purposes. Colors correspond to regions 1:cyan, 2:gray, 3:magenta, 4:blue, 5:black, 6:green, 7:red, 8:orange 9:dark gray as defined in Figure 8 and Table 1. Note the high flux above ∼2.0 keV in the spectrum of regions 7−9 indicating a strong hard spectral component. The different relative strengths of emission lines among the various regions are due, in part, to real differences in elemental abundances as the best-fitting models all have similar plasma temperatures and absorption columns (Table 1).

The first thermal component temperature is typically $kT \sim 0.5$ to 0.8 keV. It was found that the second component usually had a steep power law slope (photon index $\Gamma \gtrsim 2.5$) or only a slightly higher temperature ($kT \sim 0.8$ to 1.0 keV) suggesting that this component may represent the range of thermal emission temperatures expected along a given line of sight through the SNR rather than a true non-thermal component typically indicated by a power law shape. This is true of most of these outlier regions except regions 7−9 where $\Gamma < 2.3$ (or $kT_2 > 3.5$ keV). In these cases, it is likely that there is truly a hard non-thermal component even if the two-kT model is formally a better fit as such high temperatures are atypical of SNR spectra. The PWN likely contributes this non-thermal emission component in regions 8 and 9 because they are immediately adjacent to the high-surface-brightness PWN.

The elemental abundances were not well constrained in any of these models but strong emission lines of H-like O and Ne, and He-like blends of Ne, Mg, Si, S are present throughout as shown in Figure 9 whereas Fe emission is weak. This is indicative of a Type II core collapse SN origin.

Overall, since the spatial scale of the observed brightness variations are of order 1′, and the spectra of the different regions sampled also vary, none of these regions (nor any other region on S3) can be safely defined as a background to be used in fitting spectra of the PWN. Thus, the "blank sky" background[17] appropriate to this observation is the only background used in subsequent spectral analysis with the exception of the pulsar, J0617, and the jet-like and ring features. For these objects, the space between the pulsar and ring is relatively faint and local backgrounds were chosen from this region.

[16] $K_{\rm POW}$ is in units of flux density, ph keV^{-1} cm^{-2} s^{-1} at 1 keV and $K_{\rm THM}$ is in units of $10^{-14}(4\pi d^2)^{-1}$ times the emission measure, in cm^{-3}.

[17] obtained from the CalDB and accessed following the CIAO science thread http://asc.harvard.edu/ciao/threads/acisbackground/

3.2.2. *Spectra and Timing of CXOU J061705.3+222127*

The spectrum of J0617 was extracted from a 2-pixel (0.984″) radius circle centered at the location of the pulsar (see also Figure 2). A nearby background was obtained by combining data from five 2-pixel radius circles located interior to the ring and excluding the jet-like features. This results in an estimated 925±35 net source counts in the 0.5−8.0 keV energy range. Absorbed blackbody and neutron star atmosphere (Pavlov et al., 1995; Zavlin, 2009) models (plus a power law component) were fit to the spectrum over the 0.5−8.0 keV energy range after grouping to ensure a minimum of 20 background-subtracted events per spectral energy bin. The spectrum, models, and fit residuals are shown in Figure 10. The neutron star atmosphere model assumed a distance to the star of 1.5 kpc, a radius $R_{\rm NS} = 10$ km, a mass $M_{\rm NS} = 1.4$ $M_\odot$ (corresponding to a gravitational redshift parameter $g_r \equiv [1 - 2GM_{\rm NS}/(R_{\rm NS}c^2)]^{1/2} = 0.766$) and a magnetic field strength of 10^{13} G.

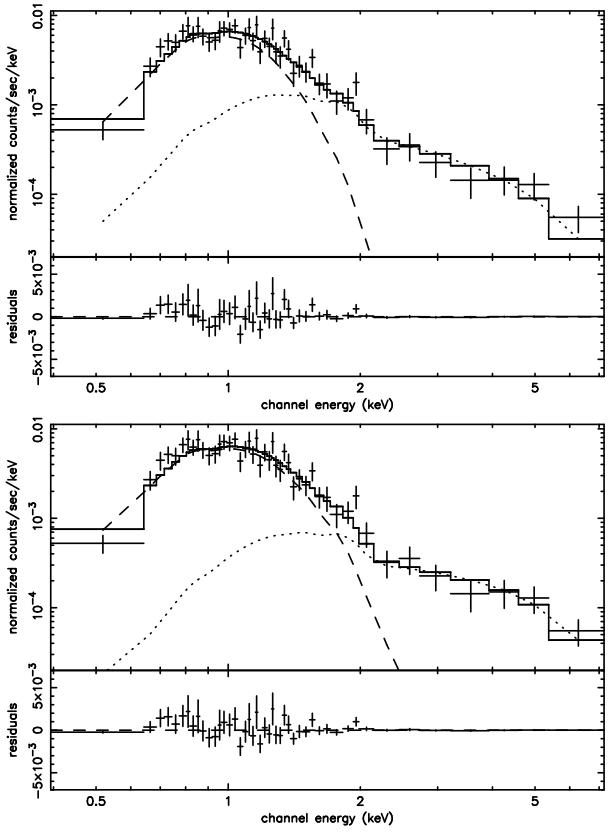

FIG. 10.— Observed spectrum of CXOU J061705.3+222127 extracted from within an ∼1″ (2-pixel) radius circle. A background, extracted from small regions surrounding the source, interior to the ring, and excluding bright regions associated with the jet-like feature, has been subtracted. The spectrum has been grouped to obtain a minimum of 20 counts per spectral bin. The solid line denotes the full model (*top:* absorbed blackbody plus power law; *bottom:* absorbed neutron star atmosphere plus power law), The dotted lines are the contributions of the power law component and the dashed lines are the blackbody (*top*) and NSA model (*bottom*) components. The lower panels show the respective fit residuals.

The best-fitting model parameters, derived properties, and fit statistics are listed in Table 2, where T^∞ and R^∞ are the effective temperature and radius as measured by a distant observer, and L_Γ is the 0.5−8.0 keV luminosity of the non-thermal (power law) component. Errors in Table 2 are at the 1σ (68%) confidence level. Both models provided acceptable fits to the data. These spectral properties are typical for a cooling neutron star although the blackbody model radius, $R^\infty = 1.63$ km, implies emission from a small hotspot rather than the entire neutron star surface. They indicate a bolometric luminosity of $(1-3)\times10^{32}$ erg s^{-1}.

A search for a possible periodicity in the X-ray flux from J0617 was restricted to periods $P > 6.5$ s due to the 3.24-s time resolution of the ACIS instrumental setup. The Rayleigh test yielded a maximum power at a period of 31.18 s. Applying the appropriate probability distribution (Groth, 1975) sets an upper limit to the power at 99% confidence that translates to an upper limit on the pulsed fraction of 36% assuming a sine-wave signal and accounting for the background.

3.2.3. *Spectra of the Jet and Ring*

The spectrum of the southern jet-like feature was extracted from a 10″×5″ region oriented N−S and centered at $06^{\rm h}17^{\rm m}5.25^{\rm s}$ +22°21′25.5″. The background-subtracted source spectrum (using the same background regions as for J0617) was grouped to a minimum of 10 events per spectral energy bin and fit using an absorbed power law. There were too few counts (233±21) to justify attempting more complex models. The best-fitting model parameters are $n_{\rm H} = 6.3^{+3.0}_{-1.2} \times 10^{21}$ cm^{-2} and $\Gamma = 1.2^{+0.4}_{-0.3}$ (χ^2/dof = 20.9/18) resulting in an absorbed 0.5−8.0 keV model flux of $2.1^{+2.8}_{-1.3}\times10^{-14}$ erg cm^{-2} s^{-1} and absorption-corrected luminosity of $7.0^{+8.0}_{-4.0} \times 10^{29} d^2_{1.5}$ erg s^{-1}. There were too few counts for spectral analysis of the northern portion of the jet.

The spectrum of the ring was extracted from a circular annulus lying between radii of 3.7″ and 5.9″ from the ring center. An absorbed power law model with parameters $n_{\rm H} = 5.2^{+0.6}_{-0.5} \times 10^{21}$ cm^{-2}, Γ=1.4±0.1 produced an acceptable fit to the spectrum (χ^2/dof = 194.3/182). The resulting 0.5−8.0 keV model flux is $(3.1\pm0.3)\times10^{-13}$ erg cm^{-2} s^{-1} and the absorption-corrected luminosity is $1.1\times10^{32} d^2_{1.5}$ erg s^{-1}.

3.2.4. *Spectra Upstream of the Pulsar Wind Nebula*

Spectra were extracted from a series of regions located upstream of the pulsar to search for a spectral transition between the non-thermal shocked PWN emission and thermal emission from shocked ambient medium further upstream. Figure 8 shows the locations of these regions. They are 40×100 pixel^2 (0.269 arcmin^2) rectangles oriented with the long side perpendicular to the line of apparent motion of the pulsar. Table 3 presents the spectral fitting results for these regions (ordered left to right by increasing distance from J0617). As with the outlier regions discussed in section 3.2.1, absorbed two-component models were applied. Both models provide similarly acceptable fits although the thermal plus power law is formally the superior model. With the exception of the region nearest to J0617, the temperature of the soft thermal component in all cases, $kT \sim 0.6 - 0.7$ keV, is consistent with the soft component deduced for the outlier regions of section 3.2.1. Most regions have an obvious hard component ($\Gamma \lesssim 2.3$ or $kT_2 > 3.5$ keV) that is poorly modeled by a second *ther-*

mal component. For the non-thermal power law (plus soft thermal) models, the trend is for the power law index to steepen and both the power law flux and its fraction of the total flux to decrease with distance from J0617. This is certainly true of the innermost three regions although the trend is less evident in the outer three regions where the power law component is much weaker though still required in the modeling. While there is no abrupt spectral transition from non-thermal- to thermal-dominated emission, a non-thermal component is clearly present at least out to $2'$ upstream from J0617, which is consistent with the smoothly-varying surface brightness distribution of this upstream region (cf. Figure 4 and section 3.1.3).

3.2.5. *Spectra of the Pulsar Wind Nebula: Contour Binning*

The contour binning method of Sanders (2006) was applied to a region containing the pulsar, PWN, and immediate surroundings as described in §2. By definition, this binning method traces the decrease in surface brightness with distance from J0617. Using this prescription, the PWN is subdivided into roughly concentric "annuli" with the innermost region containing J0617, the ring and the jet. The outermost of these regions is indicated in Figure 8 by the thick irregular contour surrounding J0617. By design, each region contains roughly 10^4 X-ray events. Because the extended thermal emission from the IC 443 SNR is so spatially non-uniform, the contour binning method did not satisfactorily bin the regions beyond the PWN.

The results of model fits to the spectra of these regions are given in Table 4 (a 3-pixel ($1.48''$) radius circle centered on J0617 was excluded from the innermost region, denoted Region 1 for spectral analysis; regions 2 through 7 lie sequentially ourward). In addition to model parameters and derived properties listed previously (Table 1 and 3), Table 4 includes fluxes, $f^{\rm cor}$, corrected for absorption along the line of sight. The spectra were fit on the extended 0.5−8.0 keV energy range and fluxes listed in Table 4 are over this same interval.

An absorbed power law model provided a statistically-superior fit to the spectra of the three innermost regions. An absorbed two-component (`powerlaw` and `vmekal` or two `vmekal`) model was needed for the outer zones but one component is always hard ($\Gamma < 2$ or $kT > 5$ keV) and dominates the 0.5−8.0 keV flux; again, indicating a true non-thermal component is present as argued in section 3.2.1. For this reason, the two `vmekal` component model is not considered further. The soft thermal component in the two-component non-thermal model is generally cooler, $kT \lesssim 0.4$ keV, throughout these PWN regions than in the 'outlier' fields (Section 3.2.1) but note that the soft component contributes at most 5% of the flux in all but the outermost PWN region. The outermost region is similar to the outlier regions 7−9 (Table 1) in that its soft thermal component temperature is 0.67 keV and its power-law index is ∼2. Unlike these outlier regions, nearly all the flux in even this outermost PWN region is provided by the non-thermal model component.

To test the significance of the low temperature in the inner zones, the fits were repeated with the `vmekal` model temperature parameter fixed to its value in the outermost zone, $kT = 0.67$ keV. This results in some additional flux in the 1-2 keV band which forces the power law index to flatten slightly to compensate. However, this is only a modest change in slope and within the errors obtained if the thermal model temperature were left as a free parameter. For example, in the fourth zone, Γ decreases from 1.9±0.1 to 1.8±0.1.

Maps of several of the resulting best-fitting model parameters are displayed in Figure 11 for the single-component absorbed `powerlaw` model. These maps show that the power law slope smoothly increases with distance from J0617, that the intensity decreases, and that the best-fitting column density is roughly constant but decreases in the outermost zone. This latter trend is perhaps influenced by the simplicity of this single-component model.

3.2.6. *Spectra of the Pulsar Wind Nebula: Comparisons to Radio Data*

The X-ray emission in the J0617 pulsar wind nebula is clearly dominated by a non-thermal component suggesting a synchrotron emission source. Radio images of the region (Olbert et al., 2001; Castelletti et al., 2011) also show a cometary morphology which may imply a similar origin. However, the radio and X-ray data have much different spatial resolution and sensitivity so that a direct comparison is non-trivial. Specifically, the signal to noise of the higher frequency radio data is too low to allow for measurements in small regions for comparison with the X-ray fluxes. Instead, by cutting the upper and lower uv range of the 4.8 GHz and 8.4 GHz measurements to a common $\sim 1.7' \times 0.77'$ region (see Figure 8) with equal coverage at both frequencies (and at 330 MHz), radio spectral index measurements of roughly the whole J0617 PWN can be obtained. Comparison of the coverage after cutting showed no apparent gaps in the coverage and thus both frequencies should be sensitive to emission over a similar range of spatial scales. The data were therefore re-imaged and convolved with a circular beam of size $8.5''$ and the images were blanked for emission falling below a three sigma cutoff before measurements were taken of the total flux of this region. This yields nearly equal fluxes at all three frequencies, 84.3±7.6, 87.6±3.0, and 87.0±0.6 mJy at 330 MHz, 4.8 GHz and 8.4 GHz, respectively, and therefore a flat spectral index of $\alpha_{\rm R} = 0.01$ in the radio band consistent with Olbert et al. (2001) and Castelletti et al. (2011).

The combined 330 MHz image does not suffer from these sensitivity issues but does not have the high spatial resolution of the X-ray data. Therefore, instead of the contour binning regions of section 3.2.5, a set of successively larger elliptical annuli approximating the innermost five contour binning regions was analyzed at both 330 MHz and X-rays. As before, the X-ray spectrum is predominantly non-thermal and a single absorbed `powerlaw` model provided an acceptable fit. Here, J0617 was *not* excluded since it cannot be cleanly masked out of the low-resolution radio image. The 330 MHz radio fluxes were calculated by integrating over each region after subtracting an estimated contribution due to emission from the surrounding SNR as noted in section 2.3. Table 5 summarizes the geometry and the radio and X-ray properties for these regions.

If the SNR-background-subtracted 330 MHz radio flux and the non-thermal (power-law component) X-ray emission arise from the same physical mechanism, then their spectral shapes should be simply related. The slopes of these spectra are obviously different: The radio spectrum,

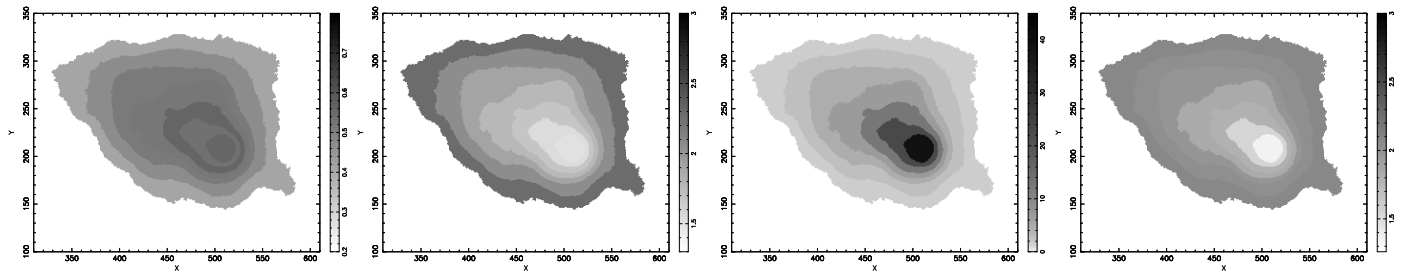

FIG. 11.— Spectral properties of the seven regions encompassing the PWN as defined by the contour binning method of Sanders (2006) and listed in Table 4. Properties are shown for the single absorbed power law model. Region numbers listed in Table 4 column headings (1−7) are ordered from the inside outward. Each region encompasses an area of approximately uniform surface brightness. The innermost (region 1) is approximately 15 pixels ($\sim$7.5″) in radius and contains the ring, and the jet features (J0617 is excluded); region 2 encompasses the "plateau" region (see Figure 4). The panels display (*clockwise from top left:*) the fitted absorption column density, $n_{\rm H}/10^{22}$ cm^2, the power law model photon index, Γ, the observed 0.5−8.0 keV intensity, $\epsilon_{\rm X}/10^{-16}$ erg cm^{-2} s^{-1} arcsec^{-2}, and the power law model normalization, $K_{\rm POW}/10^{-4}$ photons kev^{-1} cm^{-2} s^{-1} at 1 keV.

$\alpha_{\rm R}$, is flat, at least on average over the entire region, while $\alpha_{\rm X} \equiv \Gamma - 1 \simeq 0.5 - 1$ depending on the (elliptical) region. For a power-law X-ray spectrum with a photon index Γ and normalization $K_{\rm POW} = 10^{-4} K_{-4}$ photons (cm^2 s keV)$^{-1}$ at $E = 1$ keV, the energy flux spectrum is $F_{\nu,{\rm X}} \propto K_{-4} \nu^{-\Gamma+1}$. Extrapolation of this X-ray spectrum towards lower frequencies intersects the extrapolation of the radio spectrum, $F_{\nu,{\rm R}} = F_{1{\rm GHz}} (\nu/1{\rm GHz})^{-\alpha_{\rm R}}$, at frequency $\tilde{\nu}$ when

$$(\alpha_{\rm X} - \alpha_{\rm R}) \log \tilde{\nu} = \log(K_{-4}/F_{1{\rm GHz}}) + 8.3838 \alpha_{\rm X} - 4.1798,$$

where $\tilde{\nu}$ is in units of GHz and $F_{1{\rm GHz}}$ is in mJy. Inserting the appropriate values from Table 5, and assuming $\alpha_{\rm R} = 0$ everywhere (and no uncertainty in the radio flux densities), the estimated frequencies $\tilde{\nu}$ are as listed in the last row of Table 5. In the X-ray hard (flat) inner elliptical regions 1 and 2, the extrapolation crosses the radio spectrum at frequencies lower than 4.8 or 8.4 GHz which means that there should be at least two breaks in a power law spectrum or the radio spectrum is not flat in those regions.

4. DISCUSSION

4.1. *Properties of the Central Source*

Deep *Chandra*/ACIS observations show the point-like object, CXOU J061705.3+222127, has an X-ray spectrum dominated by a thermal component with parameters typical of a cooling neutron star. The fit with a hydrogen atmosphere (NSA) model shows an effective temperature $T_{\rm eff}^{\infty} \approx 6.8 \times 10^5$ K and a bolometric luminosity $L_{\rm bol}^{\infty} \approx 2.6 \times 10^{32}$ erg s^{-1} (see Table 2). Such temperature and luminosity are very close to those obtained from the NSA fit of the thermal component of the Vela pulsar (Pavlov et al., 2001), whose age τ is about 20–30 kyr, larger than the characteristic spin-down age $\tau_{\rm sd} \equiv P/2\dot{P} = 11$ kyr (Lyne et al., 1996). Similar temperature and luminosity for $\tau \sim 30$ kyr were obtained in some neutron star cooling models (e.g., Page et al., 2009). Therefore, we can expect that age of the neutron star in J0617 is a few times 10^4 yr. It is consistent with the IC 443 age ~ 30 kyr estimated by Chevalier (1999), although some authors inferred much younger ages for this SNR (e.g., Petre et al. (1988) suggested $\tau \sim 3$ kyr).

Compared to the NSA model, the blackbody fit of the thermal component gives a higher temperature, $T_{\rm BB} \approx 1.5 \times 10^6$ K, and a smaller radius, $R_{\rm BB} \approx 1.6 d_{1.5}$ km, similar to the Vela pulsar. Such emission could emerge from a hot spot on the neutron star surface heated by precipitation of relativistic particles from the pulsar magnetosphere, or it could reflect strong nonuniformity of the surface temperature due to anisotropy of heat conductivity of the neutron star crust caused by very strong magnetic fields (see, e.g., Geppert & Viganò, 2014). The non-detection of pulsations with $P > 6.5$ s does not contradict the small size of the emitting region because such young pulsars have much shorter periods[18].

Since the NSA and blackbody models yield fits of about the same quality, we cannot prefer one model to the other based solely on the observations. However, the NSA fit looks somewhat more preferable because it gives reasonable cooling neutron star properties at the expected SNR age and distance.

The detection of the nonthermal power-law component in the neutron star spectrum and the presence of the nonthermal X-ray nebula around the neutron star show that CXOU J061705.3+222127 is a rotation-powered pulsar. The nonthermal component, presumably emitted from the pulsar's magnetosphere, dominates the pulsar spectrum at $E \gtrsim 1.7$ keV. The spectral slope and the "isotropic luminosity" of the nonthermal component ($L_\Gamma \equiv 4\pi d^2 f_{\rm pl}^{\rm cor}$) are also close to those of the Vela pulsar[19], for both thermal component models used in fit.

Since pulsations have not been detected, we do not know the pulsar's spin-down properties, $\dot{E}$ and $\tau_{\rm sd}$. We, however, can constrain them from a comparison of the PWN 0.5–8 keV luminosity $L_{\rm pwn} \approx 1.4 \times 10^{33} d_{1.5}^2$ erg s^{-1} (given by the sum of the non-thermal components of the 7 contour-binning regions of Section 3.2.5) with the X-ray luminosities of PWNe produced by pulsars with known $\dot{E}$ and $\tau_{\rm sd}$. Assuming $d_{1.5} = 1$ and using Figure 5 from Kargaltsev & Pavlov (2008), Figure 2 from Li et al. (2008), and Figure 3 from Kargaltsev et al. (2012), we obtain a range of possible spin-down luminosities $\dot{E} \approx$ (1–

[18] Periods larger than 6.5 s are observed in magnetars, but this neutron star does not show any magnetar properties.

[19] Note a typo in Pavlov et al. (2001): The power-law luminosities in Table 1 should be in units of 10^{31} (not 10^{32}) erg s^{-1}.

30) $\times 10^{36}$ erg s^{-1}, with the most likely value around 3×10^{36} erg s^{-1}. Similarly, using Figure 5 from Li et al. (2008), we obtain a range of possible spin-down ages, $\tau_{\rm sd} \sim$ 10–100 kyr, with the most likely value around 20 kyr, consistent with the age estimates from the properties of the thermal component. From these estimates we obtain constraints on the period, $P \sim$ 0.1–0.6 s, and the surface magnetic field, $B \sim (0.4–4) \times 10^{13}$ G, with most likely values around 0.25 s and 2×10^{13} G, respectively.

Note that the true pulsar's X-ray luminosity is apparently much higher than the above-estimated L_Γ because the (distance-independent) ratio $L_{\rm pwn}/L_\Gamma \sim$ 100–200 is much larger than for any known pulsar-PWN pair (see Figure 5 in Kargaltsev & Pavlov, 2008). This suggests that the pulsar beam misses the Earth, which could also be the explanation for non-detection of the pulsar in the radio and γ-rays.

J0617 is separated from the apparent center of the IC 443 SNR by 15′ in a direction nearly due south. This corresponds to a projected length $s_\perp = 2 \times 10^{19} d_{1.5}$ cm and a projected velocity $v_\perp = 640\, d_{1.5} \tau_4^{-1}$ km s^{-1}. This is below the observed upper limit (Section 3.1.1) of $310\, d_{1.5}$ km s^{-1} if $\tau_4 \equiv \tau/10^4\,{\rm yr} \gtrsim 2$, which is consistent with the possible IC 443 age and the spin-down age estimated above from the empirical $L_{\rm pwn}$–$\tau_{\rm sd}$ correlation. The true speed is $v_{\rm psr} = v_\perp (\sin i)^{-1}$, where i is the angle between the direction of motion and the line of sight. Observed pulsar speeds range up to ∼1000 km s^{-1} (e.g., Arzoumanian et al., 2002) which constrains the angle: $\sin i \gtrsim 0.64 \tau_4^{-1} d_{1.5}$, assuming J0617 was born in the center of IC 443 (e.g., $i \gtrsim 19°$ for $\tau_4 \sim 2$, $d_{1.5} = 1$). The angle i is larger for more typical pulsar velocities – for instance, $32° \lesssim i \lesssim 53°$ for $v = 400$ km s^{-1} and a reasonable age range $2 \lesssim \tau_4 \lesssim 3$, at $d_{1.5} = 1$.

4.2. *The surrounding medium*

All regions imaged by *Chandra* surrounding J0617 and its PWN have a strong thermal emission component, likely emitted from the IC 443 SNR. This likely means that J0617 lies within this warm plasma, but a simple line-of-sight projection cannot be ruled out (and, thus, the distance to J0617 remains unknown). The typical temperature of this warm plasma is $kT \sim 0.7$ keV (Section 3.2.1) corresponding to a sound speed, $c_s = (\gamma kT/\mu m_H)^{1/2} \approx 430\,(kT/0.7\,{\rm keV})^{1/2}(0.6/\mu)^{1/2}$ km s^{-1} for a $\gamma = 5/3$ gas and molecular weight $\mu \simeq 0.6$, appropriate for fully-ionized medium with roughly cosmic abundances. Thus, if J0617 is within this plasma and not just lying along the same line of sight, then the pulsar motion cannot be highly supersonic; the Mach number $\mathcal{M} = v_0/c_s \lesssim 2.3$ for $v_0 < 10^3$ km s^{-1}. Here, v_0 is the speed with respect to the ambient medium; $v_0 \sim v_{\rm psr}$ in the absence of any bulk motions in the plasma. Whether the speed is supersonic, transonic, or subsonic has a strong bearing on the shape of the nebula (which is also influenced by its orientation relative to the line of sight) and the properties of the particle and electromagnetic field flow within the nebula. This is addressed in more detail in Section 4.3.

Assuming, for the present, that J0617 and its PWN are embedded in the IC 443 SNR, the ambient thermal pressure, $p_{\rm thm} = \rho(kT/\mu m_H)$, where ρ is the ambient mass density, can be estimated with the aid of the `vmekal` model fit parameters. The `vmekal` model norm is $K_{\rm THM} = 10^{-14}(4\pi d^2)^{-1} \int n_e n_H dV \simeq 10^{-14}(4\pi d^2)^{-1} n_H^2 V$, where n_H is the hydrogen number density, and V is the volume of the emitting region. The volume can be expressed in terms of the area A of the region image (in arcmin^2) and the average depth l_{19} (in units of 10^{19} cm) of the region along the line of sight: $V = 1.8 \times 10^{55} A l_{19} d_{1.5}^2$ cm^3. Using this expression for V and assuming that fully ionized hydrogen gives the main contribution, the hydrogen number density and the ambient thermal pressure can thus be estimated as follows:

$$n_H = 0.39\, K_{-4}^{1/2} (A l_{19})^{-1/2}\ {\rm cm}^{-3}\,,$$

$$p_{\rm thm} \simeq 2 n_H kT = 0.92 \times 10^{-9} K_{-4}^{1/2} (A l_{19})^{-1/2}\, kT\ {\rm dyn\,cm}^{-2}\,,$$

where $K_{\rm THM} = 10^{-4} K_{-4}$ and kT is in units of keV.

The n_H and $p_{\rm thm}$ estimates are proportional to $l_{19}^{-1/2}$, which depend on the SNR geometry and the J0617 position within the SNR. J0617 lies, in projection, about 15′ ($2 \times 10^{19} d_{1.5}$ cm) from the center of the ∼ 20′ radius IC 443 remnant (assuming a spherical remnant). Thus, a chord through the remnant along the line of sight to J0617 should have a length of about 2×10^{19} cm or less, so typical expected values are $l_{19} \sim 1$ (corresponding to ∼ 7.5′ in the sky plane).

Using the values from spectral fits to the nine outlier regions, Table 1, the mean hydrogen densities (and standard deviations) for the low- and high-temperature `vmekal` components are $n_H/l_{19}^{-1/2} = 0.5 \pm 0.1$ and 0.6 ± 0.2 cm^{-3}. The corresponding pressures are $p_{-9}/l_{19}^{-1/2} = 0.7 \pm 0.2$ for the low-temperature component (where $p_{\rm thm} = 10^{-9} p_{-9}$ dyn cm^{-2}). For the high-temperature component in regions 1 through 6 the pressures are 1.4 ± 0.4, but they average 5 ± 2 for regions 7 through 9 because of the much higher temperatures determined for those regions, averaging 4 keV compared to only 0.8 keV for the high-temperature component in regions 1−6 (and 0.6 keV for the low-temperature component in all regions).

4.3. *Morphology of the Ring and Cometary Nebula*

The cometary shape observed from many PWNe is generally attributed to motion of the system relative to the ambient medium. In the case of powerful, young, subsonically-moving pulsars such as the Crab, a distinct jet-torus structure may be present near the pulsar related to axial symmetry in the wind caused by rotation of the pulsar. In other systems, particularly older pulsars moving supersonically through a cold interstellar medium, the PWN structure consists of a forward bowshock and an extended tail.

J0617 appears to have some attributes of both these extremes. It has a distinct, nearly circular, ∼5″-radius circumstellar ring encircling jet-like features and a ∼2′×1.5′ comet-shaped nebula. In analogy to the Crab, the ring may define a termination shock (TS) where the ultrarelativistic free-flowing equatorial wind slows to subrelativistic speeds, referred to as the inner ring in the Crab (Weisskopf et al., 2000), or the ring may be a torus of shocked pulsar wind similar to the one that lies some distance beyond the inner ring of the Crab. Since in both cases the symmetry axis of the J0617 ring should be the spin axis of the pulsar, the ellipticity of the ring implies

the angle ζ between the line of sight and the spin axis is about 30° (see Section 3.1.2). If we assume that the spin axis coincides with the direction of motion, similar to many other pulsars (Johnston et al., 2005), and J0617 originated at the center of IC 443, then the pulsar velocity can be estimated as $v_{\rm psr} \sim 400$–600 km s^{-1}, for $d_{1.5} = 1$ and $\tau_4 \sim 2$–3 (see Section 4.1), comparable to the speed of sound in the ambient medium estimated in Section 4.2. The relatively small ζ value corresponds to a distance from the SNR center to the pulsar of $s \sim 4 \times 10^{19} d_{1.5}$ cm. This requires the SNR must be elongated along the line of sight if J0617 is still within the SNR. For instance, if the SNR is a prolate spheroid whose polar axis is parallel to the line of sight, then this axis must be a factor of 2 longer than the equatorial radius and the length of the chord through the SNR along the line of sight to J0617 becomes $l_{19} \sim 7 d_{1.5}$ (cf. Section 4.2).

In this geometry the north-south jet-like features could be true pulsar jets (e.g., similar to the inner jets of the Vela pulsar; Pavlov et al., 2003) of $\sim 10^{17} d_{1.5}$ cm (deprojected) length. The fact that the southern jet is brighter than the northern jet can be explained by the Doppler boosting, i.e., the outflow in the southern jet is approaching the observer, which implies that the pulsar is also approaching and located in the front part of the SNR. The offset of the apparent ring center from the pulsar (see Figure 3) could be explained similar to that of the Crab inner ring (Weisskopf et al., 2012), e.g., as caused by an intrinsic azimuthal asymmetry due to nonuniformity of the ambient medium or even a simple geometric displacement caused by a non-equatorial ring.

In this interpretation the observed X-ray PWN beyond the ring is comprised of a shocked pulsar wind outflow. Its cometary shape is formed by the ram pressure caused by the motion of J0617 relative to the ambient medium. The misalignment of $\sim 50°$ between the symmetry axis of the comet-shaped PWN and the direction toward the SNR center could be explained by bulk motion of the SNR matter in the vicinity of J0617 with a velocity of a few hundred km s^{-1} (e.g., due east or east-southeast).

We should note that the ellipticity of the J0617 ring derived from the image analysis (Section 3.1.2) is subject to large systematic uncertainties due to the ring faintness and the (apparent) ring-jet intersections. Therefore, we cannot exclude the possibility that the true ellipticity is much smaller than 30°, i.e., the ring is nearly circular. In this case, if we assume that the pulsar's spin axis is aligned with direction of motion, we would have to conclude that J0617 could *not* originate at the center of the IC 443 SNR. However, if we allow a strong misalignment between the spin axis and the direction of motion (e.g., similar to IGR J11014–6103; Pavan et al., 2014), then the circular shape of the ring would not impose restrictions on the direction of motion and birthplace of the pulsar. Nevertheless, if the jet-like features are indeed the jets, they would lie nearly along the line of sight and would be exceptionally long. Thus, some ellipticity of the ring is required if it is associated with the equatorial pulsar wind.

The cometary shape of the larger PWN may offer some additional guidance in interpreting the observed properties of J0617. In general, the pulsar wind flows non-radiatively until it encounters the TS, while the shocked pulsar wind, confined between the TS and a contact discontinuity (CD) that separates the shocked pulsar wind from shock-heated ambient material, emits synchrotron radiation. The shapes of the TS, CD and the outer (forward) shock, which separates the shocked ambient gas from unshocked ambient gas, depend on the Mach number.

In the supersonic case, $\mathcal{M} \gg 1$, the shapes of these surfaces ahead of the moving pulsar resemble paraboloids whose sky projections look bow-like if the angle between the pulsar velocity and the line of sight is large enough. The shocked pulsar wind at the bow apex is confined in a thin layer, and thus the TS and CD surfaces upstream from the central source are close to each other, $R_{\rm TS}(\theta) \sim R_{\rm CD}(\theta)$ at $\theta \ll 1$, where θ is the polar angle with respect to the symmetry axis of the flow. The TS standoff distance can be estimated from the balance between the bulk wind pressure inside the TS and the ram pressure of the ambient matter:

$$\dot{E}/[4\pi c R_{\rm TS}^2(\theta=0)] \sim \rho v_0^2 \qquad (1)$$

(assuming the pulsar wind is isotropic inside the TS). At arbitrary θ the pressure balance defines a surface $R_{\rm TS}(\theta)$. An analytical solution for $R_{\rm TS}(\theta)$ was derived by Wilkin (1996) in the thin-layer approximation, it agrees well with numerical simulations (e.g., Bucciantini et al., 2005) for small θ and high $\mathcal{M}$. For $\theta \ll 1$, the Wilkin formula can be approximated by the parabola $(y/R_0) = C(x/R_0)^2 + 1$ with $C = 0.3$, where $R_0 = R_{\rm TS}(0)$, $-y$ is along the direction of motion, $(x/y) = \tan\theta$, and the pulsar is at the focus $x = y = 0$. Although the head of the observed cometary PWN resembles a parabola, the fit to the X-ray contours in Section 3.1.3 gives a substantially larger coefficient of the quadratic term, $C = 0.54$ instead of 0.3. The sharper (narrower) head of the observed PWN[20] and the smooth surface brightness profile ahead of the pulsar (i.e., the lack of any structure that could be identified with a TS; see Figure 5) provides additional evidence that the pulsar motion is not supersonic.

In the transonic case, $\mathcal{M} \sim 1$, the ambient thermal pressure contributes, in addition to the ram pressure, to the right hand side of Equation (1). Since $c_s^2 = \gamma p_{\rm thm}/\rho$, the total pressure can be written as $p_{\rm thm} + \rho v_0^2 = \rho v_0^2 (1 + \gamma^{-1}\mathcal{M}^{-2})$, and the stand-off distance for the CD can be estimated as $R_{\rm CD}(0) \sim R_{\rm TS}(0) \sim \dot{E}^{1/2}(4\pi c \rho v_0^2)^{-1/2}(1 + \gamma^{-1}\mathcal{M}^{-2})^{-1/2} \sim 10^{17}(\dot{E}/3 \times 10^{36}\,{\rm erg\,s^{-1}})^{1/2} p_{-9}^{-1/2}(1 + \gamma\mathcal{M}^2)^{-1/2}$ cm. Inserting plausible parameter values for the pulsar and the ambient medium (estimated in Sections 4.1 and 4.2), $R_{\rm CD}(0) \sim 10^{17}$ cm which corresponds to $4.5'' d_{1.5}^{-1}$ or roughly the observed ring radius. In this transonic case, there is no longer a general analytic solution, but the parabolic approximation for the CD head at $\gamma\mathcal{M}^2 \gtrsim 0.7$ gives $C \approx 0.3 + 0.2(\gamma\mathcal{M}^2)^{-1}$. It becomes close to the measured $C = 0.54$ at $\gamma\mathcal{M}^2 \approx 0.8$, or $\mathcal{M} \approx 0.7$ for $\gamma = 5/3$.

In the subsonic limit, $\mathcal{M} \ll 1$, the canonical bow-shock model must be abandoned because the thin layer assumption, $R_{\rm TS} \sim R_{\rm CD}$, does not apply even in the forward direction. Instead, the flow can be treated as incompressible so that Laplace's equation for the veloc-

[20] Note that the parabola becomes even 'wider' if there is a component of the motion along the line of sight, $i < 90°$.

ity field, with appropriate boundary conditions, correctly describes the hydrodynamics. Near the pulsar, the flow is again idealized as purely radial, whereas at large distances the velocity must be uniform and directed opposite the direction of motion of the pulsar. The solution is then the sum of a uniform flow and a radial flow from the pulsar with speed falling as the square of the radius. Since the post-shock radial velocity component must be about $c/3$ at the TS outer boundary (Kennel & Coroniti, 1984) but $\sim v_0 \ll c/3$ at the CD (where the two velocity components cancel), $R_{\rm TS}(0) \ll R_{\rm CD}(0)$, and the CD standoff distance is $R_{\rm CD}(0) = (c/3v_0)^{1/2} R_{\rm TS}(0) \simeq 18(v_0/300\,{\rm km\,s^{-1}})^{-1/2} R_{\rm TS}(0)$. We do not clearly see the CD in our images, perhaps because it is blurred by instabilities. However, if we assume $R_{\rm CD}(0) \sim 15''$–$30''$(see Figures 5 and 6), then the above estimate gives $R_{\rm TS}(0) \sim 1''$–$2''$(for $v_0 = 300$ km s^{-1}), much smaller than the ring radius, $\sim 5''$. This means the ring may be analogous to the Crab's torus while the TS may be hidden in the wings of the pulsar's PSF (see Figure 2). Note that the relative motion cannot be highly subsonic for reasonable estimates of v_0 since $c_s \sim 400$ km/s.

The overall shape of the PWN also depends on the Mach number. In the supersonic and transonic regimes, numerical solutions (Bucciantini et al., 2005) show the $R_{\rm TS}(\theta)$ surface develops a bullet shape with the TS elongated in the downstream direction ($\theta = \pi$) and terminating in a Mach disk oriented perpendicular to the direction of motion. Simulations show the ratio $R_{\rm TS}(\pi)/R_{\rm TS}(0) \sim (1+\mathcal{M}^2)^{1/2}$ for lower $\mathcal{M}$, reaching a limit of $\sim$5 for $\mathcal{M} \gg 1$. This amount of elongation is incompatible with observations of J0617, again suggesting the flow is not supersonic. Note that a circular ring is only conceivable if the pulsar wind was purely radial producing a limb-brightened spherical emission region outside the TS. However, pulsar winds are known to be highly aspherical resulting in emission morphologies like the Crab torus. As we mentioned above, if the ring is a torus, then the spin axis is predominantly along the line of sight.

Finally, in the supersonic and transonic regimes, the expected shocked pulsar wind speeds in the tail (roughly along the CD) are 0.3–$0.5c$ (Bucciantini et al., 2005), whereas they are only of order $v_0 \sim 300$ km s^{-1} in the subsonic case. Particles in this flow will only radiate at X-ray energies, $E \sim 1$ keV, for a time $\tau \sim 200(E/1\,{\rm keV})^{-1/2}(B/50\,\mu{\rm G})^{-3/2}$ yr due to their synchrotron losses. Here, B is the equipartition magnetic field defined (Pacholczyk, 1970) as $B = (6\pi c_{12}(1+k)L/(fV))^{2/7}$ where f is the filling factor in a volume V producing a synchrotron luminosity L over some spectral range, c_{12} a constant dependent on this spectral range and the spectral slope (index), and the ion to electron energy ratio $k = 0$ for a pure pair plasma. From the flux density in the radio band, $\sim$86 mJy (section 3.2.6), a volume of that region of 10^{54} cm^3 assuming a filled prolate ellipsoid, and a flat radio spectrum extending to 100 GHz ($c_{12} = 7 \times 10^6$), the field strength is $B \sim 65(\sin i)^{2/7}$ μG. The length of the J0617 nebular tail extends roughly $1.5'$ or $2 \times 10^{18} d_{1.5} (\sin i)^{-1}$ cm implying a velocity of $\sim 500(\sin i)^{-5/7}$ km s^{-1} for this synchrotron age. This is somewhat larger than the subsonic velocity estimate and only approaches the transonic velocity estimate as $i \to 0°$.

In summary, the shape of the forward region of the J0617 PWN and the size of its surrounding ring implies a transonic (or mildly subsonic) net flow because of the additional flow collimation that occurs at low $\mathcal{M}$. The size of the circular ring is compatible with the standoff distance of a termination shock unless the flow is subsonic in which case the ring is larger than the TS by a factor of 20 or so. In any case, the near circularity of the ring implies either emission from a limb-brightened spherical emission region or emission from a toroidal region with symmetry axis nearly along the line of sight. Neither of these two conclusions is satisfactory, however, as the former belies the known predominantly azimuthal emission geometry associated with rotating magnetized neutron stars and the latter implies a pulsar orientation unlikely to produce the observed shape of the larger cometary PWN.

Acknowledgments

The *Chandra* observations were obtained in response to Chandra Proposal Number 13500093 by the Chandra X-ray Observatory Center, which is operated by the Smithsonian Astrophysical Observatory for and on behalf of the National Aeronautics Space Administration under contract NAS8-03060. Optical observations were obtained with the SARA Observatory 0.9 m telescope at Kitt Peak, which is owned and operated by the Southeastern Association for Research in Astronomy. Basic research in radio astronomy at the Naval Research Laboratory (TC) is supported by 6.1 Base funding.

References

Anders, E., & Grevesse, N. 1989, Geochim. Cosmochim. Acta, 53, 197

Arnaud, K. A. 1996, Astronomical Data Analysis Software and Systems V, 101, 17

Arzoumanian, Z., Chernoff, D. F., & Cordes, J. M. 2002, ApJ, 568, 289

Bocchino, F. & Bykov, A. M. 2000, A&A, 362, L29

Bocchino, F. & Bykov, A. M. 2001, A&A, 376, 248

Bucciantini, N. 2002a, A&A, 387, 1066

Bucciantini, N., Amato, E., & Del Zanna, L. 2005, A&A, 434, 189

Castelletti, G., Dubner, G., Clarke, T., & Kassim, N. E. 2011, A&A, 534, AA21

Chevalier, R. A. 1999, ApJ, 511, 798

Gaensler, B. M., Chatterjee, S., Slane, P. O., et al. 2006, ApJ, 648, 1037

Gaensler, B. M., & Slane, P. O. 2006, ARA&A, 44, 17

Geppert, U., & Viganò, D. 2014, MNRAS, 444, 3198

Groth, E. J. 1975, ApJS, 29, 285

Johnston, S., Hobbs, G., Vigeland, S., et al. 2005, MNRAS, 364, 1397

Kargaltsev, O. & Pavlov, G. G. 2008, 40 Years of Pulsars: Millisecond Pulsars, Magnetars and More, AIP Conference Proceedings, 983, 171

Kargaltsev, O., Pavlov, G. G., & Durant, M. 2012, Electromagnetic Radiation from Pulsars and Magnetars, 466, 167

Kennel, C. F., & Coroniti, F. V. 1984, ApJ, 283, 694

Keohane, J. W., Petre, R., Gotthelf, E. V., Ozaki, M., & Koyama, K. 1997, ApJ, 484, 350

Lee, J.-J., Koo, B.-C., Yun, M. S., Stanimirović, S., Heiles, C., & Heyer, M. 2008, AJ, 135, 796

Li, X.-H., Lu, F.-J., & Li, Z. 2008, ApJ, 682, 1166

Lyne, A. G., Pritchard, R. S., Graham-Smith, F., & Camilo, F. 1996, Nature, 381, 497

Monet, D. G., Levine, S. E., Canzian, B., et al. 2003, AJ, 125, 984

Olbert, C. M., Clearеld, C. R., Williams, N. E., et al. 2001, ApJ, 554, L205

Pacholczyk, A. G. 1970, Series of Books in Astronomy and Astrophysics, San Francisco: Freeman

Page, D., Lattimer, J. M., Prakash, M., & Steiner, A. W. 2009, ApJ, 707, 1131

Pavan, L., Bordas, P., Pühlhofer, G., et al. 2014, A&A, 562, AA122

Pavlov, G. G., Shibanov, Y. A., Zavlin, V. E., & Meyer, R. D. 1995, NATO Advanced Science Institutes (ASI) Series C, 450, 71

Pavlov, G. G., Zavlin, V. E., Sanwal, D., Burwitz, V., & Garmire, G. P. 2001, ApJ, 552, L129

Pavlov, G. G., Teter, M. A., Kargaltsev, O., & Sanwal, D. 2003, ApJ, 591, 1157

Petre, R., Szymkowiak, A. E., Seward, F. D., & Willingale, R. 1988, ApJ, 335, 215

Sanders, J. S. 2006, MNRAS, 371, 829

Tennant, A. F. 2006, AJ 132, 1372

Weisskopf, M. C., Hester, J. J., Tennant, A. F., et al. 2000, ApJ, 536, L81

Weisskopf, M. C., Elsner, R. F., Kolodziejczak, J. J., O'Dell, S. L., & Tennant, A. F. 2012, ApJ, 746, 41

Welsh, B. Y. & Sallmen, S. 2003, A&A, 408, 545

Wilkin, F. P. 1996, ApJ, 459, L31

Zavlin, V. E. 2009, Astrophysics and Space Science Library, 357, 181

TABLE 1
OUTLIER REGIONS SPECTRAL FIT PARAMETERS

Region[a]	1	2	3	4	5	6	7	8	9
Area (arcmin^2)	4.75	1.96	1.53	3.80	2.95	4.23	5.07	2.02	3.03
Absorbed (Power Law + Variable MeKaL)[b]									
$n_{\rm H}/10^{22}$ (cm^2)	$0.49^{+0.03}_{-0.05}$	$0.37^{+0.03}_{-0.04}$	$0.64^{+0.05}_{-0.12}$	$0.51^{+0.04}_{-0.03}$	$0.48^{+0.04}_{-0.07}$	$0.48^{+0.03}_{-0.04}$	$0.58^{+0.06}_{-0.06}$	$0.48^{+0.09}_{-0.05}$	$0.45^{+0.03}_{-0.03}$
Γ	$2.99^{+0.33}_{-0.62}$	$4.14^{+1.03}_{-0.77}$	$3.52^{+0.60}_{-0.60}$	$3.91^{+0.51}_{-0.30}$	$3.52^{+0.68}_{-1.18}$	$3.50^{+0.30}_{-0.36}$	$2.17^{+0.10}_{-0.11}$	$1.95^{+0.10}_{-0.09}$	$2.26^{+0.12}_{-0.17}$
kT (keV)	$0.69^{+0.02}_{-0.02}$	$0.70^{+0.03}_{-0.01}$	$0.79^{+0.05}_{-0.16}$	$0.69^{+0.02}_{-0.02}$	$0.68^{+0.03}_{-0.02}$	$0.66^{+0.02}_{-0.02}$	$0.68^{+0.03}_{-0.02}$	$0.78^{+0.06}_{-0.06}$	$0.68^{+0.02}_{-0.02}$
$K_{\rm POW}/10^{-4}$	$1.41^{+0.99}_{-0.92}$	$0.04^{+0.04}_{-0.04}$	$1.30^{+0.73}_{-0.96}$	$2.66^{+1.51}_{-0.96}$	$0.85^{+0.63}_{-0.80}$	$1.71^{+0.63}_{-0.95}$	$3.34^{+0.48}_{-0.45}$	$2.06^{+0.27}_{-0.26}$	$2.45^{+0.42}_{-0.51}$
$K_{\rm THM}/10^{-4}$	$12.10^{+5.11}_{-2.48}$	$8.20^{+3.26}_{-2.19}$	$3.26^{+3.52}_{-2.28}$	$8.34^{+3.38}_{-3.71}$	$3.01^{+1.64}_{-1.16}$	$3.57^{+3.01}_{-0.23}$	$2.88^{+1.09}_{-0.35}$	$0.87^{+2.47}_{-0.15}$	$4.16^{+8.03}_{-0.51}$
$f_{\rm POW}/10^{-13}$ ([c])	1.60	0.30	0.88	1.75	0.70	1.42	7.58	6.23	5.43
$f_{\rm THM}/10^{-13}$	8.59	6.74	1.57	6.43	2.68	4.31	3.18	1.04	5.32
χ^2/dof	356.6/238	251.0/180	176.6/161	346.4/222	314.2/188	359.7/220	507.0/278	307.9/259	381.9/262
Absorbed (Variable MeKaL + Variable MeKaL)[d]									
$n_{\rm H}/10^{22}$ (cm^2)	$0.47^{+0.04}_{-0.05}$	$0.33^{+0.03}_{-0.03}$	$0.53^{+0.15}_{-0.10}$	$0.47^{+0.07}_{-0.05}$	$0.45^{+0.08}_{-0.09}$	$0.48^{+0.06}_{-0.06}$	$0.56^{+0.05}_{-0.06}$	$0.49^{+0.09}_{-0.08}$	$0.46^{+0.04}_{-0.04}$
kT_1 (keV)	$0.60^{+0.04}_{-0.04}$	$0.65^{+0.03}_{-0.03}$	$0.50^{+0.07}_{-0.07}$	$0.60^{+0.04}_{-0.04}$	$0.56^{+0.08}_{-0.08}$	$0.55^{+0.05}_{-0.04}$	$0.64^{+0.02}_{-0.02}$	$0.64^{+0.05}_{-0.05}$	$0.67^{+0.02}_{-0.02}$
kT_2 (keV)	$0.78^{+0.02}_{-0.02}$	$0.74^{+0.15}_{-0.02}$	$1.02^{+0.26}_{-0.09}$	$0.80^{+0.11}_{-0.05}$	$0.77^{+0.11}_{-0.05}$	$0.82^{+0.09}_{-0.05}$	$3.55^{+0.36}_{-0.30}$	$4.72^{+0.78}_{-0.50}$	$3.75^{+1.00}_{-0.51}$
$K_1/10^{-4}$	$3.19^{+3.18}_{-0.29}$	$2.68^{+6.32}_{-0.57}$	$4.27^{+2.65}_{-2.56}$	$7.44^{+6.40}_{-4.07}$	$1.72^{+1.57}_{-1.08}$	$3.60^{+3.07}_{-1.38}$	$6.81^{+1.95}_{-1.77}$	$2.98^{+1.07}_{-0.89}$	$7.39^{+4.43}_{-1.85}$
$K_2/10^{-4}$	$16.86^{+6.05}_{-9.10}$	$9.13^{+2.60}_{-7.19}$	$6.69^{+1.56}_{-2.44}$	$12.19^{+4.94}_{-7.16}$	$6.18^{+3.37}_{-3.37}$	$6.60^{+1.94}_{-3.09}$	$7.10^{+1.06}_{-1.33}$	$5.68^{+0.50}_{-1.01}$	$4.01^{+1.09}_{-0.87}$
$f_1/10^{-13}$	2.52	2.39	0.70	3.37	0.88	2.32	3.43	1.22	5.97
$f_2/10^{-13}$	7.41	4.37	1.70	4.73	2.43	3.28	7.09	5.87	4.79
χ^2/dof	323.1/238	239.7/180	150.1/161	327.3/222	305.3/188	317.5/220	414.5/278	280.1/259	374.4/262

[a]Numbers correspond to the numbered regions shown in Figure 8

[b]Abundances tied to solar ratios for the groups CNO, Ne and Mg, Si and S, and Fe and Ni.

[c]All fluxes in units of erg cm^{-2} s^{-1}.

[d]Same as (b) and abundances of second MeKaL model tied to those of first model.

TABLE 2
SPECTRAL FIT PARAMETERS & DERIVED QUANTITIES FOR CXOU J061705.3+222127

Model	$n_{\rm H}$ 10^{22} cm^{-2}	T^∞ eV	R^∞ km	$L^\infty_{\rm bol}$ 10^{32} erg s^{-1}	Γ	L_Γ 10^{31} erg s^{-1}	χ^2/dof
NSA	$0.63^{+0.02}_{-0.03}$	$58.4^{+0.6}_{-0.4}$	13.05	2.6±0.1	$1.34^{+0.31}_{-0.35}$	$1.0^{+1.4}_{-0.5}$	42.2/42
BB	$0.61^{+0.13}_{-0.09}$	$132.0^{+8.8}_{-7.0}$	$1.63^{+0.09}_{-0.07}$	$1.0^{+0.2}_{-0.1}$	$2.00^{+0.30}_{-0.20}$	$1.4^{+0.6}_{-0.5}$	41.7/41

TABLE 3
UPSTREAM SPECTRAL FIT PARAMETERS

Region[a]	1	2	3	4	5	6
Absorbed (Power Law + Variable MeKaL)[b]						
$n_{\rm H}/10^{22}$ (cm^2)	$0.61^{+0.09}_{-0.08}$	$0.40^{+0.06}_{-0.04}$	$0.40^{+0.06}_{-0.05}$	$0.40^{+0.05}_{-0.05}$	$0.40^{+0.08}_{-0.06}$	$0.37^{+0.06}_{-0.05}$
Γ	$2.08^{+0.15}_{-0.15}$	$2.13^{+0.23}_{-0.24}$	$2.19^{+0.27}_{-0.28}$	$2.59^{+0.39}_{-0.38}$	$2.41^{+0.44}_{-0.47}$	$2.43^{+0.41}_{-0.42}$
kT (keV)	$0.39^{+0.10}_{-0.05}$	$0.70^{+0.06}_{-0.09}$	$0.67^{+0.07}_{-0.10}$	$0.72^{+0.12}_{-0.04}$	$0.68^{+0.07}_{-0.08}$	$0.71^{+0.10}_{-0.09}$
$K_{\rm POW}/10^{-5}$	$6.50^{+1.15}_{-0.98}$	$3.01^{+0.87}_{-0.71}$	$2.45^{+0.82}_{-0.66}$	$2.39^{+1.01}_{-0.78}$	$1.59^{+0.89}_{-0.66}$	$1.62^{+0.79}_{-0.61}$
$K_{\rm THM}/10^{-5}$	$7.12^{+3.76}_{-2.53}$	$3.79^{+0.93}_{-0.79}$	$2.91^{+0.79}_{-0.70}$	$2.75^{+0.71}_{-0.64}$	$3.32^{+0.81}_{-0.71}$	$2.65^{+0.68}_{-0.59}$
$f_{\rm POW}/10^{-13}$ (erg cm^{-2} s^{-1})	1.60	0.78	0.60	0.41	0.32	0.32
$f_{\rm THM}/10^{-13}$ (erg cm^{-2} s^{-1})	0.26	0.31	0.23	0.22	0.26	0.23
χ^2/dof	135.5/146	120.1/116	111.7/ 99	97.8/ 90	58.6/ 84	66.5/ 80
Absorbed (Variable MeKaL + Variable MeKaL)[c]						
$n_{\rm H}/10^{22}$ (cm^2)	$0.63^{+0.10}_{-0.09}$	$0.71^{+0.10}_{-0.13}$	$0.79^{+0.14}_{-0.11}$	$0.37^{+0.06}_{-0.04}$	$0.40^{+0.06}_{-0.06}$	$0.36^{+0.07}_{-0.05}$
kT_1 (keV)	$0.38^{+0.06}_{-0.05}$	$0.32^{+0.07}_{-0.03}$	$0.29^{+0.04}_{-0.05}$	$0.71^{+0.05}_{-0.03}$	$0.67^{+0.06}_{-0.07}$	$0.70^{+0.07}_{-0.09}$
kT_2 (keV)	$4.16^{+1.04}_{-0.70}$	$2.55^{+0.51}_{-0.39}$	$2.40^{+0.56}_{-0.38}$	$3.37^{+1.43}_{-1.09}$	$4.37^{+8.06}_{-1.67}$	$3.63^{+3.23}_{-1.23}$
$K_1/10^{-4}$	$0.90^{+0.54}_{-0.31}$	$1.31^{+0.81}_{-0.59}$	$1.65^{+2.24}_{-0.71}$	$0.33^{+0.07}_{-0.04}$	$0.39^{+0.08}_{-0.07}$	$0.30^{+0.07}_{-0.07}$
$K_2/10^{-4}$	$1.36^{+0.11}_{-0.10}$	$0.87^{+0.08}_{-0.10}$	$0.69^{+0.08}_{-0.07}$	$0.31^{+0.08}_{-0.05}$	$0.23^{+0.07}_{-0.06}$	$0.24^{+0.07}_{-0.06}$
$f_1/10^{-13}$ (erg cm^{-2} s^{-1})	0.31	0.30	0.24	0.28	0.31	0.26
$f_2/10^{-13}$ (erg cm^{-2} s^{-1})	1.54	0.74	0.55	0.36	0.29	0.29
χ^2/dof	144.1/146	134.0/116	115.2/ 99	107.9/ 90	65.5/ 84	72.3/ 80

[a]Regions upstream (southwest) of J0617 (see Figure 8), numbered by increasing distance from J0617.

[b]Abundances fixed to those of Outlier region 6 (see Table 1.

[c]Same as (b) and abundances of second MeKaL model tied to those of first model.

TABLE 4
PULSAR WIND NEBULA SPECTRAL FIT PARAMETERS

Region[a]	1	2	3	4	5	6	7
Area (arcmin^2)	0.048	0.091	0.157	0.266	0.365	0.531	0.722
				Absorbed Power Law			
$n_{\rm H}/10^{22}$ (cm^2)	$0.56^{+0.04}_{-0.04}$	$0.53^{+0.03}_{-0.03}$	$0.56^{+0.04}_{-0.03}$	$0.52^{+0.03}_{-0.03}$	$0.51^{+0.03}_{-0.03}$	$0.47^{+0.03}_{-0.03}$	$0.41^{+0.02}_{-0.02}$
Γ	$1.50^{+0.06}_{-0.03}$	$1.54^{+0.06}_{-0.05}$	$1.69^{+0.06}_{-0.03}$	$1.78^{+0.06}_{-0.06}$	$1.91^{+0.06}_{-0.06}$	$2.06^{+0.06}_{-0.06}$	$2.28^{+0.07}_{-0.07}$
$K_{\rm POW}/10^{-4}$	$1.35^{+0.10}_{-0.09}$	$1.54^{+0.11}_{-0.10}$	$1.79^{+0.13}_{-0.11}$	$1.84^{+0.12}_{-0.12}$	$1.98^{+0.14}_{-0.13}$	$2.02^{+0.14}_{-0.13}$	$2.08^{+0.14}_{-0.13}$
$f_{\rm POW}/10^{-13}$ (erg cm^{-2} s^{-1})	6.84	7.56	7.20	6.72	6.20	5.42	4.61
$f^{\rm cor}_{\rm POW}/10^{-13}$ (erg cm^{-2} s^{-1})	9.14	10.11	10.21	9.71	9.40	8.61	7.78
χ^2/dof	289.2/293	336.7/302	278.9/295	326.5/285	294.4/282	353.2/274	375.6/254
				Absorbed (Power Law + Variable MeKaL)[b]			
$n_{\rm H}/10^{22}$ (cm^2)	$0.64^{+0.35}_{-0.07}$	$0.67^{+0.25}_{-0.16}$	$0.75^{+0.28}_{-0.11}$	$0.77^{+0.18}_{-0.15}$	$0.67^{+0.18}_{-0.10}$	$0.60^{+0.15}_{-0.09}$	$0.47^{+0.09}_{-0.07}$
Γ	$1.55^{+0.09}_{-0.04}$	$1.53^{+0.03}_{-0.03}$	$1.77^{+0.14}_{-0.13}$	$1.89^{+0.05}_{-0.11}$	$1.95^{+0.12}_{-0.09}$	$2.03^{+0.12}_{-0.09}$	$1.97^{+0.10}_{-0.09}$
kT (keV)	$0.11^{+0.15}_{-0.03}$	$0.36^{+0.06}_{-0.28}$	$0.36^{+5.12}_{-0.10}$	$0.32^{+0.09}_{-0.04}$	$0.29^{+0.04}_{-0.05}$	$0.37^{+0.03}_{-0.06}$	$0.67^{+0.11}_{-0.06}$
$K_{\rm POW}/10^{-4}$	$1.46^{+0.31}_{-0.13}$	$1.49^{+0.47}_{-0.47}$	$2.05^{+0.45}_{-0.37}$	$2.20^{+0.36}_{-0.33}$	$2.14^{+0.36}_{-0.71}$	$1.98^{+0.33}_{-0.23}$	$1.41^{+0.47}_{-0.16}$
$K_{\rm THM}/10^{-4}$	$69.94^{+3837.17}_{-69.89}$	$1.02^{+6.70}_{-1.02}$	$0.35^{+4.52}_{-0.27}$	$0.79^{+7.59}_{-0.48}$	$1.89^{+8.93}_{-1.37}$	$0.69^{+3.03}_{-0.24}$	$0.61^{+1.14}_{-0.12}$
$f_{\rm POW}/10^{-13}$ (erg cm^{-2} s^{-1})	6.81	7.56	6.99	6.44	5.98	5.20	4.10
$f_{\rm THM}/10^{-13}$ (erg cm^{-2} s^{-1})	0.00	0.00	0.16	0.24	0.21	0.28	0.70
$f^{\rm cor}_{\rm POW}/10^{-13}$ (erg cm^{-2} s^{-1})	9.40	10.10	10.85	10.60	9.81	8.62	6.39
$f^{\rm cor}_{\rm THM}/10^{-13}$ (erg cm^{-2} s^{-1})	0.80	0.08	2.03	3.57	2.46	1.62	1.98
χ^2/dof	284.8/287	336.7/301[c]	267.2/289	298.0/279	258.8/276	276.3/268	215.5/248
				Absorbed (Variable MeKaL + Variable MeKaL)[d]			
$n_{\rm H}/10^{22}$ (cm^2)	$0.54^{+0.07}_{-0.05}$	$0.53^{+0.07}_{-0.06}$	$0.65^{+0.18}_{-0.14}$	$0.51^{+0.15}_{-0.05}$	$0.69^{+0.08}_{-0.15}$	$0.44^{+0.10}_{-0.04}$	$0.41^{+0.07}_{-0.06}$
kT_1 (keV)	$0.08^{+79.82}_{-0.00}$	$1.03^{+78.87}_{-0.79}$	$0.63^{+0.19}_{-0.24}$	$0.46^{+0.16}_{-0.13}$	$0.71^{+0.07}_{-0.05}$	$0.41^{+0.35}_{-0.04}$	$0.65^{+0.06}_{-0.06}$
kT_2 (keV)	$14.70^{+4.27}_{-3.12}$	$23.60^{+56.30}_{-19.58}$	$9.11^{+2.85}_{-1.61}$	$7.86^{+1.65}_{-1.37}$	$7.98^{+2.20}_{-1.80}$	$4.98^{+1.18}_{-0.58}$	$5.37^{+1.23}_{-0.81}$
$K_1/10^{-4}$	$305.73^{+342.30}_{-305.73}$	$1.67^{+2.49}_{-1.67}$	$1.59^{+2.67}_{-1.27}$	$1.83^{+5.53}_{-1.32}$	$3.35^{+1.72}_{-1.66}$	$2.22^{+3.76}_{-1.16}$	$2.69^{+1.85}_{-1.01}$
$K_2/10^{-4}$	$5.73^{+0.40}_{-0.95}$	$5.95^{+0.34}_{-5.95}$	$5.67^{+0.72}_{-1.61}$	$5.89^{+0.44}_{-0.36}$	$4.44^{+0.92}_{-0.87}$	$5.25^{+0.37}_{-0.52}$	$3.81^{+0.35}_{-0.40}$
$f_1/10^{-13}$ (erg cm^{-2} s^{-1})	0.38	0.91	1.70	0.75	4.25	1.02	2.18
$f_2/10^{-13}$ (erg cm^{-2} s^{-1})	6.35	6.62	5.41	5.84	1.97	4.30	2.54
$f^{\rm cor}_1/10^{-13}$ (erg cm^{-2} s^{-1})	0.38	0.91	1.70	0.75	4.25	1.02	2.18
$f^{\rm cor}_2/10^{-13}$ (erg cm^{-2} s^{-1})	8.74	9.11	9.44	8.63	7.65	6.96	5.32
χ^2/dof	280.0/287	337.3/296	266.0/289	301.4/279	254.2/276	277.5/268	212.4/248

[a]Regions ordered outward from J0617 numbering 1 through 7, respectively.

[b]Abundances tied to solar ratios for the groups CNO, Ne and Mg, Si and S, and Fe and Ni.

[c]Abundances frozen to best-fit values before errors on free parameters estimated.

[d]Same as (b) and abundances of second MeKaL model tied to those of first model.

TABLE 5
PULSAR WIND NEBULA X-RAY & RADIO SPECTRAL FIT PARAMETERS

Region[a]	1	2	3	4	5
Area (arcmin^2)	0.05	0.10	0.14	0.22	0.34
$n_{\rm H}/10^{22}$ (cm^2)	$0.40^{+0.03}_{-0.03}$	$0.53^{+0.04}_{-0.03}$	$0.57^{+0.03}_{-0.03}$	$0.52^{+0.03}_{-0.03}$	$0.51^{+0.03}_{-0.03}$
Γ	$1.47^{+0.05}_{-0.05}$	$1.61^{+0.06}_{-0.06}$	$1.73^{+0.06}_{-0.06}$	$1.81^{+0.06}_{-0.06}$	$1.93^{+0.06}_{-0.06}$
$K_{\rm POW}/10^{-4}$	$1.38^{+0.08}_{-0.08}$	$1.58^{+0.12}_{-0.11}$	$1.77^{+0.13}_{-0.12}$	$1.64^{+0.12}_{-0.11}$	$1.88^{+0.13}_{-0.12}$
$f_{\rm POW}/10^{-13}$ (erg cm^{-2} s^{-1})	7.67	7.02	6.74	5.76	5.73
$f^{cor}_{\rm POW}/10^{-13}$ (erg cm^{-2} s^{-1})	9.65	9.61	9.73	8.42	8.76
χ^2/DOF	299.6/305	271.8/289	274.1/285	285.5/269	370.3/268
$f_{\rm 330MHz}$ (mJy)	5.0±0.9	11.0±3.1	11.5±5.6	10.5±8.4	18.0±13.0
$\tilde{\nu}$ (GHz)	$0.02^{+0.16}_{-0.02}$	$1.12^{+5.1}_{-1.0}$	27^{+66}_{-20}	128^{+218}_{-88}	826^{+945}_{-479}

[a]Elliptical annuli numbered from inner to outer 1 to 5